

# **Distorted propagation, dispersed sensitivities and enhanced refocusing of seismic waves in heterogeneous solids**

Yingzi Ying<sup>1,2</sup> and Christopher J. Bean<sup>2,1</sup>

<sup>1</sup>*Seismology Laboratory, School of Earth Sciences, University College Dublin, Dublin, Ireland*

<sup>2</sup>*Geophysics Section, School of Cosmic Physics, Dublin Institute for Advanced Studies, Dublin, Ireland*

## **SUMMARY**

We demonstrate some phenomena associated with the seismic waves in heterogeneous solids. The random velocity fluctuations are characterized by the von-Kármán autocorrelation functions with different standard deviations. Both P-SV and SH waves in 2D space are studied to represent the cases of the body and surface waves, respectively. The spectral-element method is adopted to perform the numerical full-waveform simulations of forward propagation, and the adjoint method is used to calculate the finite-frequency traveltime sensitivity kernels. We show that the seismic waves are highly distorted propagating in the heterogeneous solids both from snapshots and seismograms. The interaction patterns between seismic waves and solids painted by the banana-doughnut traveltime sensitivity kernels appear more dispersed increasing the heterogeneities, and the seismic waves are more sensitive to shear velocity than compressional velocity in heterogeneous solids. We back-play the recorded displacement signals into the heterogeneous solids to refocus seismic waves with an elastic time reversal mirror. The results indicate the focal spot size can be more tighter when the solids become more heterogeneous, which is the so-called super-resolution phenomenon that the Fresnel diffraction limit is transcended. The outgoing seismic waves can touch a wider area in heterogeneous solids, and the time-

reversed and back-propagated seismic waves can trace back in a multi-directional ways that the mirror plays the role with a larger effective aperture.

**Key words:** Seismic waves in heterogeneous solids, finite-frequency kernels, elastic time-reversal mirror, computational seismology

## 1 INTRODUCTION

The interior of the solid Earth is heterogeneous over all scales from global (Dziewonski & Woodhouse 1987; Trampert & Woodhouse 1995), continental (Fichtner et al. 2010; Zhu et al. 2012), regional (Hards et al. 1995; Wegler & Lühr 2001), local (Warren et al. 1963; Alpay et al. 1972), to small rock (Rubino & Holliger 2012), and even further down. The heterogeneities of solid medium have most influence when the characteristic scale is in the similar scale as a wavelength (Sato et al. 2012). The velocity inhomogeneities speed up and slow down the wave propagation in different region thus the shapes of wave trains will be distorted. The incident compressional wave or shear wave can be scattered to compressional and shear waves hitting the region with velocity fluctuations (Aki 1992), so there are continuously mutual conversions between two different types of waves in heterogeneous solid. From the tail of recorded seismogram we can observe the codas, which are the superpositions of incoherent waves scattered by randomly distributed heterogeneities and look like a random signals with gradually decreasing envelop (Aki 1969).

To reveal how the seismic waves transmit from source to receiving array and interact with heterogeneous solid, i.e., the sensitivities of the observations to the medium parameters such as compressional and shear wave velocities, we will illustrate with the banana-doughnut traveltime sensitivity kernels with the adjoint method by performing the forward and adjoint simulations, and interacting the forward and adjoint wavefields (Tromp et al. 2005; Liu & Tromp 2006; Peter et al. 2011). Instead of drawing the infinite-frequency rays, the finite-frequency kernels have a banana shape with a hollow like doughnut in cross-section, which incorporate the traveltime effects associated with wavefront healing and are frequency-dependent. The sensitivities associated with the corresponding seismogram can paint an intuitive pictures showing how seismic waves propagate, get diffracted and scattered in heterogeneous solid.

Time reversal mirror (Fink & Prada 2001; Fink 2008a), which is a generalization of phase-conjugation (Porter 1989), broadcasts the recorded broadband signals in the inverse time order. Its capability to refocus the divergent waves brings many important applications in medical ultrasonics (Fink 1992; Thomas et al. 1996), underwater acoustics (Jackson & Dowling 1991; Kuperman et al. 1998), non-destructive testing (Prada et al. 1991; Chakroun et al. 1995), and geophysics (Larmat et al.

2006; O'Brien et al. 2011), etc. In randomly heterogeneous fluids, the studies (Derode et al. 1995; Tsogka & Papanicolaou 2002; Fink 2008b) have shown that acoustic reversal mirror can refocus sound waves more tightly thus breaks through the Fresnel diffraction limitation, and such super-resolution phenomenon has been theoretically analysed in acoustics (Blomgren et al. 2002; Borcea et al. 2003; Papanicolaou et al. 2004). In this work, we will also investigate the refocusing enhancement of seismic waves in heterogeneous solid media with an elastic time reversal mirror.

In this paper, following the introduction part, we first present a heterogeneous velocity model, and compare the forward propagation of seismic waves in the homogeneous and heterogeneous solids. Then the banana-doughnut traveltime sensitivity kernels will be shown to illustrate the interaction between seismic waves and heterogeneous solids with increasing fluctuations. Next, we give the elastic time-reversal refocusing results in heterogeneous solids. At last we conclude the paper with discussion. Mathematically, we formulate the problems with general 3D elasticity, but present numerical results in 2D space. The numerical simulations include the cases of P-SV and SH waves.

## 2 PROPAGATION DISTORTION

### 2.1 Construction of heterogeneous solids

The physical properties of a heterogeneous solid in which seismic waves propagate can mainly be described by the parameters of mass density, compressional wave and shear wave velocities, without considering attenuation. Here each parameter of a heterogeneous solid is taken as a random field, which can be characterized by a spatial statistical distribution, superimposed on a smooth background. We first construct the shear wave velocity field as the function of a spatial point

$$\beta(\mathbf{x}) = \beta_0 [(\gamma(\mathbf{x}) + \xi(\mathbf{x}))], \quad (1)$$

where  $\beta_0$  is the mean value of shear wave velocity,  $\gamma$  is a deterministic smooth background, which can be a constant, a gradient, or a more general field with unit mean value, and the random variable  $\xi$  is a relative perturbation term, which characterize the random fluctuation of shear wave velocity. The perturbation term is mean-zero, i.e., the first-order statistical moment equals

$$\mathbb{E} [\xi(\mathbf{x})] = 0, \quad (2)$$

where  $\mathbb{E}$  is the expected value operator.

The spatial random perturbation of velocity field can be described by a monotonically decaying autocorrelation function, which statistically measures the spatial correlation, i.e., the similarity of values at different points over a spatial lag, as well as the fluctuation magnitude. It is defined as a

second-order statistical moment

$$R(\mathbf{y}) = \mathbb{E}[\xi(\mathbf{x})\xi(\mathbf{x} + \mathbf{y})]. \quad (3)$$

When the spatial lag vector  $\mathbf{y}$  is shortened to zero, the autocorrelation function is given as the variance

$$\sigma^2 = \mathbb{E}[\xi^2(\mathbf{x})], \quad (4)$$

and  $\sigma$  is the standard deviation, which denotes the magnitude of random fluctuation.

Equivalently, the autocorrelation function can also be expressed in the wavenumber domain using the multi-dimensional Fourier transform

$$S(\mathbf{k}) = \int d\mathbf{y} R(\mathbf{y}) e^{-i\mathbf{k} \cdot \mathbf{y}}, \quad (5)$$

as the spectral density function, whose square root characterizes the response of a wavenumber filter. Here  $\mathbf{k}$  is the wave vector.

Some commonly used autocorrelation function for modelling random velocity are the Gaussian, exponential, and von-Kármán types. The von-Kármán function, which is a generalization to the exponential function with an adjustable exponent, was first introduced by von Kármán (1948) for characterizing random velocity of turbulence. The random velocity characterized by von-Kármán autocorrelation function is self-similar and has rich components in short wavelength scale, and is commonly used to model geological structures (Sato et al. 2012). We adopt the 2D isotropic version of the von-Kármán type autocorrelation function in our simulations, whose corresponding power spectral density function is directly proportional to

$$S(\mathbf{k}) \propto \frac{1}{(1 + k^2 a^2)^{\nu+1}}, \quad (6)$$

where  $k = \|\mathbf{k}\|$  is the wavenumber,  $a$  is the isotropic correlation length, and  $\nu$  is the Hurst number.

To build the random perturbation field of shear wave velocity, a noise spectrum is first generated, get multiplied with the square root of the power spectral density function, and at last an inverse Fourier transformation is applied. The shear wave velocity perturbation field can be mathematically expressed as

$$\xi(\mathbf{y}) = \text{Re}[\int d\mathbf{k} N(\mathbf{k}) \sqrt{S(\mathbf{k})} e^{i\mathbf{k} \cdot \mathbf{y}}], \quad (7)$$

and the noise field in the wavenumber domain

$$N(\mathbf{k}) \sim \mathcal{U}(-1/2, 1/2), \quad (8)$$

is in uniform distribution.

In Fig. 1, a realization of the 2D shear wave velocity is plotted. We set the background velocity as

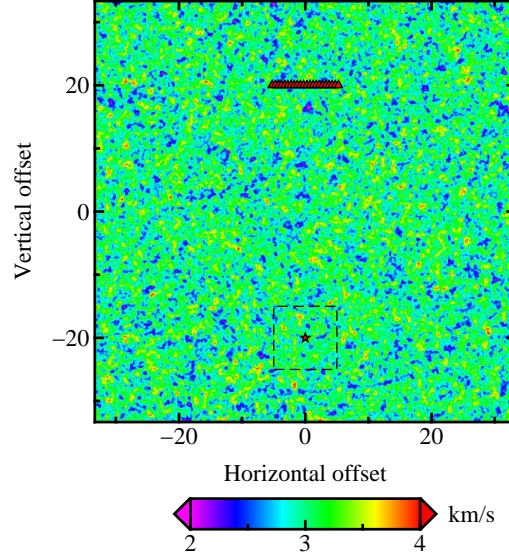


**Figure 1.** Realization of random shear velocity with 12% relative standard deviation. The dimensionless horizontal and vertical offsets are normalized by a dominant shear wavelength. The source and the receiver array are denoted as the red star and the red triangles, respectively, and the dashed-line rectangle is drawn to indicate the subregion.

a constant, that is  $\beta_0 = 3$  km/s and  $\gamma(\mathbf{x}) = 1$ , the dimensionless correlation length to  $a = 1/3$ , that is a half shear wavelength, and the Hurst number to  $\nu = 0.2$ . Here all the spatial lengths are dimensionless, which are scaled by a dominant shear wavelength  $\lambda_0$ , with respect to the central frequency of source signal  $f_0$ , i.e.,  $\lambda_0 = \beta_0/f_0$ . The results will be compared between the models with different velocity fluctuations, i.e., by setting the relative standard deviations to the values of  $\sigma/\beta_0 = 0\%$ ,  $4\%$ ,  $8\%$ , and  $12\%$ , respectively.

We just assume the Poisson ratio of the heterogeneous solids to be a constant of  $1/4$ , thus have the compressional wave velocity is linearly scaled to the shear wave velocity

$$\alpha(\mathbf{x}) = \sqrt{3}\beta(\mathbf{x}). \quad (9)$$

The mass density distribution structure here is simply given as

$$\rho(\mathbf{x}) = 1.7 + 0.2\alpha(\mathbf{x}), \quad (10)$$

in  $\text{g/cm}^3$  by using the linear version of the relationship between compressional wave velocity and density given by Gardner et al. (1974).

The seismic waves propagate through heterogeneous solid and get scattered due to the velocity heterogeneities. The relative size between the correlation length and the dominant wavelength, i.e., the dimensionless wavenumber  $ka$ , characterizes the scattering properties. In our cases, the size of the heterogeneities are comparable with the dominant wavelength of compressional wave or shear wave,

thus the dimensionless wavenumber is within the resonant scattering regime (Wu et al. 1989). In such regime the scattering effects are most significant, the incident seismic waves can be scattered to the different directions with a large angle relative to the incidence, and a lot codas can be generated.

## 2.2 Governing equations of P-SV and SH waves

We perform numerical simulations of seismic waves propagating in the heterogeneous solids, and take the P-SV and SH waves in a 2D cases as examples. Here we summarize the equations governing the generation and propagation of the seismic waves.

In a general anelastic solid, the displacement wavefield  $\mathbf{u}(\mathbf{x}, t)$  satisfies the generalized momentum equation

$$\rho \partial_{tt} \mathbf{u} - \nabla \cdot \boldsymbol{\sigma} = \mathbf{f}, \quad (11)$$

where  $\mathbf{f}$  is a simple point source due to an external force, and  $\boldsymbol{\sigma}$  is the stress. The stress  $\boldsymbol{\sigma}$  and the strain  $\boldsymbol{\epsilon}$ , which are the symmetric second-order tensors, are linearly related by the generalized Hooke's law

$$\boldsymbol{\sigma} = \mathbf{c} : \boldsymbol{\epsilon}, \quad (12)$$

where the colon operator denotes the tensor's inner product. The fourth-order stiffness tensor  $\mathbf{c}$  has 21 independent parameters, which accommodate the elastic anisotropy. The strain  $\boldsymbol{\epsilon}$  can be given in terms of the displacement gradient with the linearization

$$\boldsymbol{\epsilon} = \frac{1}{2} [\nabla \mathbf{u} + (\nabla \mathbf{u})^t], \quad (13)$$

where  $t$  is the matrix transpose operator.

In our numerical models the solid media are elastically isotropic, thus the constitutive relationship of Eq. (12) can be expressed in terms of the lamé constant and the shear modulus

$$\boldsymbol{\sigma} = \lambda \text{tr}(\boldsymbol{\epsilon}) \mathbf{1} + 2\mu \boldsymbol{\epsilon}, \quad (14)$$

where  $\mathbf{1}$  is the second-order identity tensor, and the lamé constant can also be related to the shear and bulk moduli as

$$\lambda = \kappa - \frac{2}{3}\mu. \quad (15)$$

Inserting Eqs (13–14) into Eq. (11), the isotropic version of the elastodynamic equation can be obtained as

$$\rho \partial_{tt} \mathbf{u} - \nabla \lambda (\nabla \cdot \mathbf{u}) - \nabla \mu \cdot [\nabla \mathbf{u} + (\nabla \mathbf{u})^t] - (\lambda + 2\mu) \nabla \nabla \cdot \mathbf{u} + \mu \nabla \times \mathbf{u} = \mathbf{f}. \quad (16)$$

Normally, if the media are assumed to be homogeneous or smooth, the gradients of medium pa-

rameters, i.e.,  $\nabla\lambda$  and  $\nabla\mu$ , are relatively trivial. Ignoring these terms we approximately get the following equation

$$\partial_{tt}\mathbf{u} - \alpha^2\nabla\nabla \cdot \mathbf{u} + \beta^2\nabla \times \nabla \times \mathbf{u} = \frac{1}{\rho}\mathbf{f}, \quad (17)$$

where the compressional and shear wave velocities have the values of

$$\alpha = \left( \frac{\lambda + 2\mu}{\rho} \right)^{\frac{1}{2}} \quad (18)$$

and

$$\beta = \left( \frac{\mu}{\rho} \right)^{\frac{1}{2}}, \quad (19)$$

respectively.

Eq. (17) governs the propagation of elastic waves in the solids with isotropic elasticity. Such solid media can support both the compressional waves and the shear waves, namely, the P-SV waves, which are the body waves in 2D case.

The compressional waves involve compressing as well as shearing processes, that is why its velocity depends both on the bulk and shear moduli. For the shear waves, which are divergence-free, i.e.,

$$\nabla \cdot \mathbf{u} = 0, \quad (20)$$

the particle motions can be divided into two components with different polarizations. If the polarization is on the plane through the propagation vectors, then the shear waves are classified as SV waves, which are just the component of P-SV waves. The shear waves with particle motions in the direction perpendicular to such plane are named as the SH waves, or membrane waves, which can be taken as an analogue for surface wave propagation on the Earth (Tanimoto 1990; Peter et al. 2007).

Together using Eq. (20) and the vector identity

$$\nabla \times \nabla \times \mathbf{u} = \nabla\nabla \cdot \mathbf{u} - \nabla^2\mathbf{u}, \quad (21)$$

Eq. (17) can further be reduced to the following equation governing the SH wave propagation

$$\partial_{tt}u - \beta^2\nabla^2u = \frac{1}{\rho}f, \quad (22)$$

where the scalars  $u$  and  $f$  are the normal components of the displacement and the external force source, respectively, and here  $\nabla$  is the surface gradient operator that performs on the plane perpendicular to the external force. We can see that only one kind of wave can be supported in the system of Eq. (22), which propagates with the shear wave velocity. Mathematically, SH wave on a 2D plane can be taken as a type of scalar wave, with the polarization perpendicular to the plane.

### 2.3 Numerical scheme

We employ the spectral element method, which is close to a continuous Galerkin technique, to solve the 2D seismic wave equations. The method was originally developed in computational fluid dynamics (Patera 1984) and has been very successfully adapted to computational seismology (Komatitsch & Vilotte 1998). The systems are formulated in the weak forms and the spatial integrations are performed based upon the Gauss-Lobatto-Legendre quadrature. The discretization can result in a diagonal mass matrix, an implicitly imposed free-surface condition, and a simple explicit time scheme (Komatitsch et al. 2005; Tromp et al. 2008). The spectral element method has the properties of good accuracy, convergence and tolerant to mesh distortion, and can be efficiently implemented in a parallel architectures, thus is the best solution for our numerical work.

In order to prevent, at least to reduce, annoying reflections from the edges of the models, thus represent a fictitious unbounded domains, the Clayton-Engquist-Stacey (Stacey 1988) and the convolutional Perfectly-Matched-Layer (Komatitsch & Martin 2007) absorbing boundary conditions are applied to the SH wave and P-SV wave simulations, respectively. The later condition was recently developed and has been available for P-SV waves, with the improved absorbing efficiency.

We use the homogeneous-element method, that each material parameter inside a spectral element is set to be a constant but varies between elements, to build the highly heterogeneous models. Such tricky processing naturally eliminates the approximation in discarding the material gradients.

### 2.4 Comparison of seismic waves propagating in homogeneous and heterogeneous solids

In this part, we illustrate the phenomena associated with the forward propagation both of SH waves and P-SV waves, by giving the snapshots and the seismograms. The results are compared between the cases of the homogeneous and heterogeneous models.

The shear wave velocity of the homogeneous model has 0% relative standard deviation, and the heterogeneous one is taken with 12% relative standard deviation, as illustrated in Fig. 1. With the dimensionless scale, the source is located at  $(0, -20)$ , and the horizontal linear array is symmetrically deployed with each receiver element at  $(-5.25 + 0.5n, 20)$ , for  $n = 0, 1, \dots, 21$ , counting from left to right. A Ricker wavelet with  $f_0$  central frequency is loaded as the source signal.

The SH waves can be excited by a normal force, that is perpendicular to the 2D plane, and the particle motions only have values in normal direction. Fig. 2 shows the snapshots of the displacement wavefields in the normal direction at 2.5s. The left side subfigure is the homogeneous case, in which the undistorted wavefront propagates with the shear wave velocity, and there is only one type of wave. In the heterogeneous case, which is shown on the right side, we can see that the wavefront is seriously distorted, and the plane is still under unsettled after the main arrival has elapsed, due to the multiple



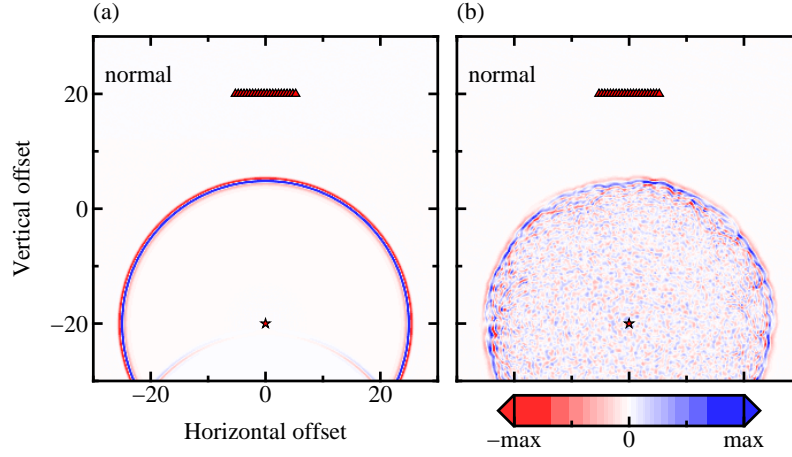


**Figure 2.** Comparison of normal displacement snapshots of SH waves at 2.5s, in the solids with (a) 0% and (b) 12% relative standard deviations. The SH waves are excited by a single force acting in the normal direction.

scattering and multiple pathing effects. The displacement signals of normal component are plotted in Fig. 3, with the wiggles of homogeneous model overlapped on the heterogeneous case. From the signals, we can also find that there is only one arrive in the homogeneous solid, but the array can record a massive codas in the heterogeneous case, and the aftersound can continue for a long time.

If we turn the single force on the 2D plane to the vertical direction, the P-SV waves can be excited. Fig. 4 shows the snapshots at 2.5s both for the models with the homogeneous and heterogeneous velocities. On the left side, the horizontal and vertical displacement snapshots are plotted on top and bottom, respectively, for the P-SV waves in the homogeneous solid, and the heterogeneous version are plotted on the right side. Both the compressional waves and the shear waves are supported here as

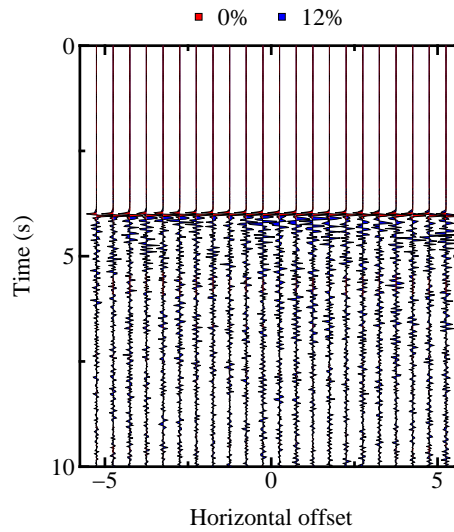


**Figure 3.** Comparison of normal displacement traces of SH waves in the homogeneous and heterogeneous solids.

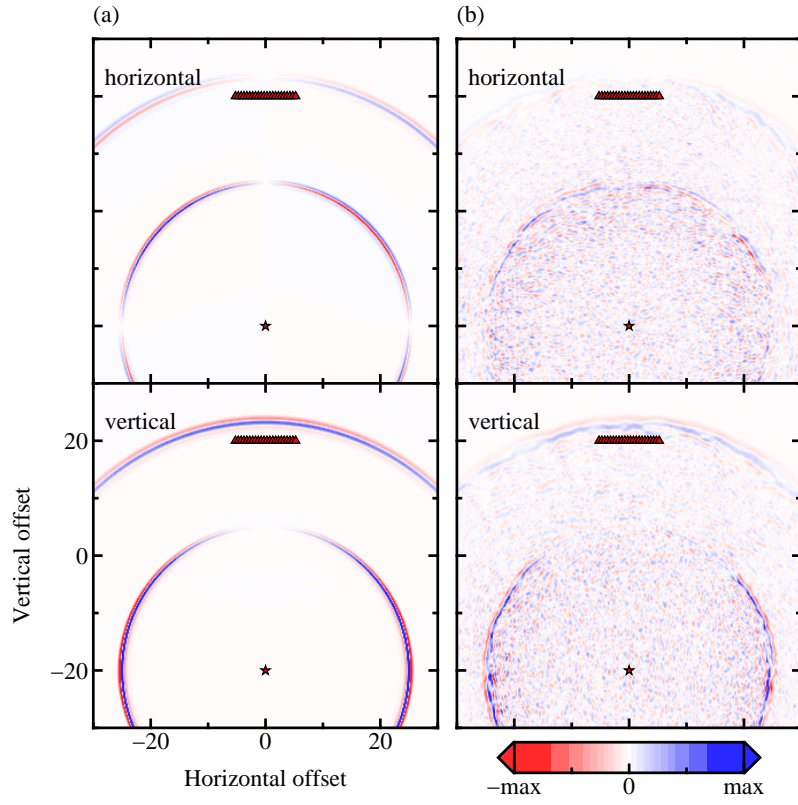


**Figure 4.** Comparison of horizontal and vertical displacement snapshots of P-SV waves at 2.5s, in the solids with (a) 0% and (b) 12% relative standard deviations. The P-SV waves are excited by a single force acting in the vertical direction.

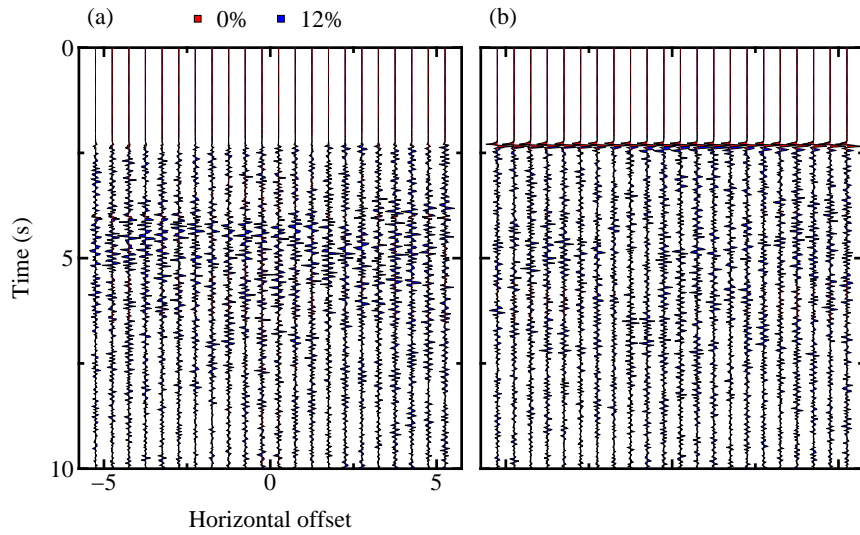


**Figure 5.** Comparison of horizontal and vertical displacement traces of P-SV waves in the homogeneous and heterogeneous solids.

seen from the wavefronts, which are seriously distorted propagating in the highly heterogeneous solid. There are complex and ceaselessly conversions between the compressional and shear waves propagating in heterogeneous solid. The horizontal and vertical displacement wiggles are plotted in Fig. 5, from which the primary and secondary arrivals can be clearly seen in the homogeneous case, but they are totally out of shape in the heterogeneous case. In highly heterogeneous solid, the compressional and shear waves are fully mixed, and the missions to pick up a distinct arrivals and make a separation between each other become extremely difficult.

### 3 SENSITIVITY DISPERSION

#### 3.1 One-to-many banana-doughnut traveltime sensitivity kernels

In tomographic inversion, the Fréchet derivative of a misfit objective function  $\chi$  can generally be expressed as

$$\delta\chi = \int d\mathbf{x} K_m(\mathbf{x}) \delta \ln m(\mathbf{x}), \quad (23)$$

where  $\delta \ln m = \delta m / m$  denotes the relative perturbation of a model parameter, and  $K_m$  is the sensitivity or Fréchet volumetric kernel.

Based on the adjoint method, a sensitivity kernel is constructed by the time-integration of the product between the regular forward wavefield and the time-reversed adjoint wavefield, or using their derivative forms. The adjoint wavefield can be generated by using a time-reversed signals at receiver positions as simultaneous sources, e.g., misfits between synthetic and observed displacements, synthetic velocities, or synthetic displacements for full waveform, traveltime, or amplitude tomography, respectively. The adjoint sources may be determined based upon the Born approximation (Tromp et al. 2005), or derived with the Lagrange multiplier method (Liu & Tromp 2006).

In this part, we calculate the banana-doughnut finite-frequency traveltime sensitivity kernels from the source to all array elements in the heterogeneous solids. For the case of traveltime sensitivity kernels, the misfit function is defined as following

$$\chi(m) = \frac{1}{2} \sum_{\mathbf{x}_r \in \mathcal{A}} \left[ T(\mathbf{x}_r, m) - T^d(\mathbf{x}_r) \right]^2, \quad (24)$$

thus its gradient has the form of

$$\delta\chi(m) = \sum_{\mathbf{x}_r \in \mathcal{A}} \left[ T(\mathbf{x}_r, m) - T^d(\mathbf{x}_r) \right] \delta T(\mathbf{x}_r, m), \quad (25)$$

where the receiver  $\mathbf{x}_r$  is in the array space  $\mathcal{A}$ , and the difference between the synthetic traveltime  $T$  and the observed traveltime  $T^d$  can be measured by the cross-correlation technique (Marquering et al. 1999). The synthetic traveltime is predicated by using a model, and the perturbation of a model

parameter  $\delta m$  will cause the perturbation of the synthetic seismogram  $\delta s$ , thus the perturbation of the synthetic traveltimes  $\delta T$ .

At a particular receiver  $\mathbf{x}_r$ , the adjoint source for the banana-doughnut traveltimes sensitivity kernel is given by the time-reversed synthetic velocity

$$\mathbf{f}^\dagger(\mathbf{x}_r, t) = \mathbf{a}_r w(-t) \partial_t \mathbf{u}(\mathbf{x}_r, -t), \quad (26)$$

here  $\mathbf{1}$  denotes the indicator function, which has a unit value at the receiver position, otherwise is zero,  $w$  is a time window, and the amplification factor is decided both by the synthetic displacement and acceleration

$$\frac{1}{\mathbf{a}_r} = \int dt w(t) \mathbf{u}(\mathbf{x}_r, t) \partial_{tt} \mathbf{u}(\mathbf{x}_r, t). \quad (27)$$

The traveltimes adjoint source, or the resulting banana-doughnut traveltimes sensitivity kernel, is independent of the data of a particular event, but just relies on the synthetic model. The observed data is only incorporated in the misfit kernel, which is the summation of banana-doughnut kernels weighted by the corresponding traveltimes differences.

In our case, we don't pick up a particular arrival of a synthetic event. In highly heterogeneous solids, a large number of codas are generated, the conversions between compressional and shear waves happen everywhere, and the waves are mixed up, thus it is difficult to separate a distinct arrival. Instead, a full time window is adopted here to include the full-scale input in each receiver, that is  $w(t) = 1$ . Also we are going to show the overall sensitivity from the source to the whole array, thus all banana-doughnut traveltimes adjoint sources are simultaneously injected at the corresponding receiver positions, that we have the adjoint source as

$$\mathbf{f}^\dagger(\mathbf{x}, t) = \mathbf{a}_r \partial_t \mathbf{u}(\mathbf{x}, -t) \mathbf{1}_{\{\mathbf{x}=\mathbf{x}_r\}}. \quad (28)$$

The kernel calculated using Eq. (28) as the adjoint source equivalents to the summation of all banana-doughnut traveltimes sensitivity kernels from the source to all array elements.

The adjoint wavefield  $\mathbf{u}^\dagger$  is simulated by using the adjoint source  $\mathbf{f}^\dagger$  as the input to the synthetic model

$$\mathcal{L} \mathbf{u}^\dagger(\mathbf{x}, t) = \mathbf{f}^\dagger(\mathbf{x}, t), \quad (29)$$

where generic wave operator  $\mathcal{L}$  denotes the P-SV or SH wave systems as given by Eq. (17) and Eq. (22), respectively. As same as the regular wavefield, the adjoint wavefield is subject to the initial conditions

$$\mathbf{u}^\dagger(\mathbf{x}, t)|_{t=0} = 0, \quad (30)$$

$$\partial_t \mathbf{u}^\dagger(\mathbf{x}, t)|_{t=0} = 0, \quad (31)$$

and the stress-free boundary condition, that the traction acting on the surface  $\partial\Omega$  vanishes

$$\mathbf{n} \cdot \boldsymbol{\sigma}^\dagger(\mathbf{x}, t)|_{\mathbf{x} \in \partial\Omega} = 0, \quad (32)$$

where  $\mathbf{n}$  denotes the unit normal vector that points outwards.

For the elastically isotropic material with the model perturbations expressed as  $(\delta\rho, \delta\kappa, \delta\mu)$ , the misfit gradient takes the form

$$\delta\chi = \sum_{m=\rho, \kappa, \mu} \int d\mathbf{x} K_m(\mathbf{x}) \delta \ln m(\mathbf{x}), \quad (33)$$

and the primary kernels of density, bulk modulus and shear modulus are given as (Tromp et al. 2005)

$$K_\rho(\mathbf{x}) = -\rho(\mathbf{x}) \int dt \mathbf{u}^\dagger(\mathbf{x}, -t) \cdot \partial_{tt} \mathbf{u}(\mathbf{x}, t), \quad (34)$$

$$K_\kappa(\mathbf{x}) = -\kappa(\mathbf{x}) \int dt e^\dagger(\mathbf{x}, -t) e(\mathbf{x}, t), \quad (35)$$

$$K_\mu(\mathbf{x}) = -2\mu(\mathbf{x}) \int dt \boldsymbol{\epsilon}^{\text{d}\dagger}(\mathbf{x}, -t) : \boldsymbol{\epsilon}^{\text{d}}(\mathbf{x}, t), \quad (36)$$

where the volumetric strain  $e$ , or equivalently, the displacement divergence

$$e = \text{tr}(\boldsymbol{\epsilon}) = \nabla \cdot \mathbf{u} \quad (37)$$

represents the change in volume per unit volume, and  $\boldsymbol{\epsilon}^{\text{d}}$  denotes the traceless strain deviator, which is

$$\boldsymbol{\epsilon}^{\text{d}} = \boldsymbol{\epsilon} - \frac{1}{3} e \mathbf{1}. \quad (38)$$

Alternatively, and seismologically more sensible, if the system is characterized in terms of density and velocities, the model perturbations become  $(\delta\rho, \delta\alpha, \delta\beta)$ , and the Fréchet derivative of the misfit objective function is given as

$$\delta\chi = \sum_{m=\rho, \alpha, \beta} \int d\mathbf{x} K_m(\mathbf{x}) \delta \ln m(\mathbf{x}), \quad (39)$$

then the secondary kernels can be derived as the linear combinations of the primary kernels

$$K'_\rho = K_\rho + K_\kappa + K_\mu, \quad (40)$$

$$K_\alpha = 2 \left( K_\kappa + \frac{4}{3} \frac{\mu}{\kappa} K_\kappa \right), \quad (41)$$

$$k_\beta = 2 \left( K_\mu - \frac{4}{3} \frac{\mu}{\kappa} K_\kappa \right), \quad (42)$$

here the alternative density kernel  $K'_\rho$  plays the same role as impedance kernel (Zhu et al. 2009), and  $K_\alpha$  and  $K_\beta$  are compressional and shear wave velocity sensitivity kernels, respectively.

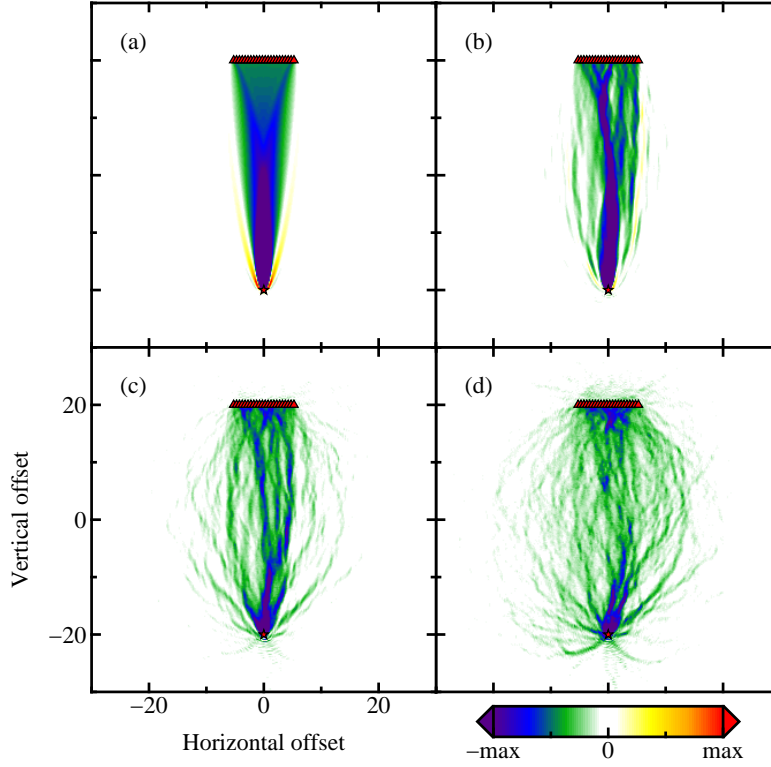


**Figure 6.** Shear wave velocity traveltime sensitivity kernels of SH waves in the solids with (a) 0%, (b) 4%, (c) 8%, and (d) 12% relative standard deviations.

### 3.2 Sensitivity anomalies in heterogeneous solids

In the part, we numerically illustrate the sensitivities of the recorded seismograms with respect to the velocity perturbations in the heterogeneous solids. With the same source and receiver deployment configurations as in the previous section about forward propagation, as well as the same source mechanism and time function, the banana-doughnut traveltime sensitivity kernels both of SH and P-SV waves are calculated and compared in the heterogeneous solids with different velocity fluctuations. The heterogeneous velocity is characterized by the von-Kármán autocorrelation functions by adjusting different standard deviation values, and a case of shear wave velocity realization with 12% relative standard deviation is plotted in Fig. 1. Two-step simulations are performed to obtain the sensitivity kernels. First a forward simulation is performed to record the synthetic seismograms, and the last frame of the displacement and velocity wavefields are saved as well. An adjoint simulation is launched by injecting the adjoint sources to calculate the adjoint wavefield, getting the synthetic regular forward wavefield simultaneously by solving the backward wave equation with the saved last snapshots as the initial conditions, and constructing the kernels from the interaction between the forward and adjoint wavefields on the fly.

We start with the SH wave cases in the 2D heterogeneous solids to simulate the surface wave sen-

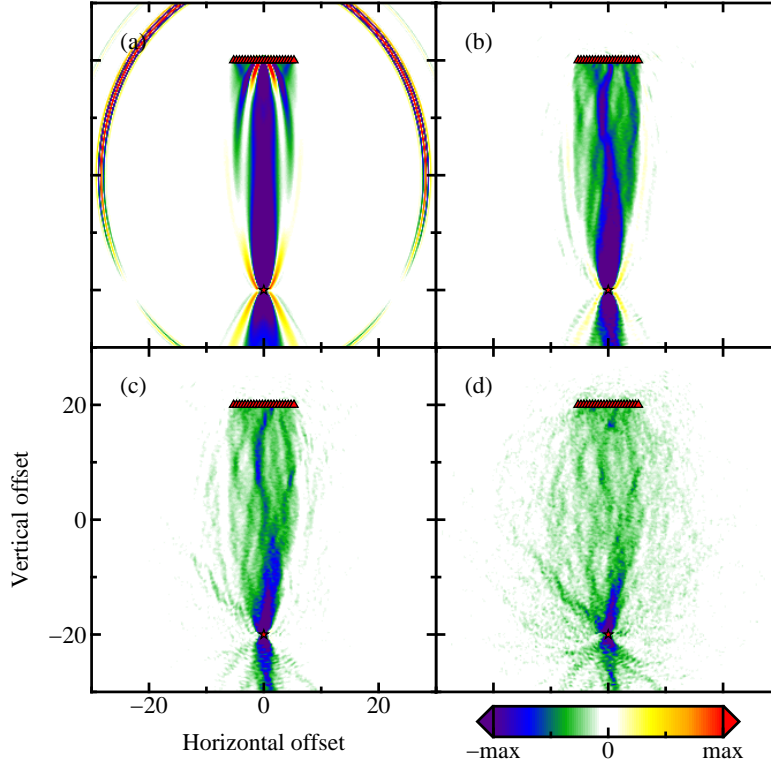


**Figure 7.** Compressional wave velocity traveltime sensitivity kernels of P-SV waves in the solids with (a) 0%, (b) 4%, (c) 8%, and (d) 12% relative standard deviations.

sensitivity dispersion. The SH wave propagation is independent of compressional wave velocity but only under the control of the shear wave velocity parameter, whose perturbation causes the seismogram distortion. The recorded normal displacements in the solids with 0% and 12% relative standard deviations are plotted in Fig. 3. The signals are time-differentiated, amplified, time-reversed and back-projected in the normal direction as the adjoint sources. Fig. 6 (a) shows shear wave velocity traveltime sensitivity kernel of SH wave in the homogeneous solid, that is 0% relative standard deviation. We can see that there is no doughnut hole here, and the kernel has negative sensitivity inside the first Fresnel zone but shifts to positive in the second Fresnel zone. The Fresnel zones, especially the first one, define the volumes in radiation pattern of wave transmission. Here as the kernel is the summation of individual kernels from the source to all receiver elements, the first Fresnel zone is also the overlapped result. Increasing the relative standard deviation to the values of 4%, 8% and 12%, the first Fresnel zone become more and more dispersed, as shown in Fig. 6 (b)-(d), respectively. The shear wave velocity perturbation causes the diffraction dispersion of the SH waves, thus can touch a more wider area and become more interactive and interfered in heterogeneous solids, and also carry more information about media on the path from source to receiver.

The P-SV wave scenario is some more complicated than the SH wave case. As observed from

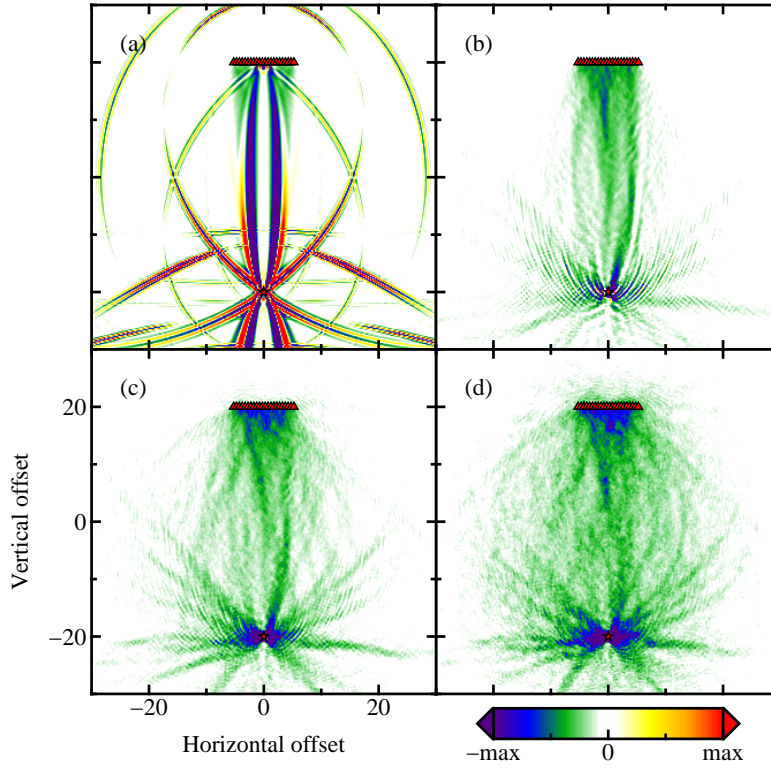


**Figure 8.** Shear wave velocity traveltime sensitivity kernels of P-SV waves in the solids with (a) 0%, (b) 4%, (c) 8%, and (d) 12% relative standard deviations.

some snapshots and seismograms as shown in Fig. 4 and Fig. 5, respectively, the particle motions of the P-SV waves in 2D solids can be decomposed in the horizontal and vertical directions, and two types of body waves exist. The propagation of P-SV wave is subject both to the compressional and shear wave velocity distributions. Converting the two-component displacements into the particle velocities as the adjoint sources, Fig. 7 depicts the compressional wave velocity sensitivity kernels of P-SV waves calculated in the solids with increasing heterogeneities. We see that there is not just the banana-doughnut feature but the hyperbolic fan tail expanding away from the source, that is because here the whole traces are taken to calculate the compressional wave velocity sensitivity kernels, which include the shear wave arrivals. The compressional wave velocity sensitivity kernels become more dispersed when the standard deviation value increases. The shear wave velocity sensitivity kernels are plotted in Fig. 8 of the solids with different standard deviations. Here the tail and slash features also show up. Comparing Fig. 7 and Fig. 8 we find that the P-SV waves propagating in the highly heterogeneous solids is more sensitive to the shear wave velocity than the compressional wave velocity structure. Similar evidence is also provided in the snapshots as shown in Fig. 4 (b). The wavefield compromised with compressional and shear waves will contain more fraction of shear waves as they are more and



more scattered by the heterogeneous region, that the codes are dominantly contained with shear waves (Aki 1980, 1992).

## 4 REFOCUSING ENHANCEMENT

### 4.1 Seismic wave refocusing with elastic time reversal mirror

Quite similar as acoustic time reversal mirror, an elastic time reversal mirror is an array compromised with transceiver elements, which are capable both to receive and transmit multi-component displacement signals. The seismic source can be an active source such as an earthquake or volcanic tremor, or a secondary source, e.g., a scatterer. The incident seismic waves imprinting on the array are recorded as displacement signals, reversed in time order, and broadcasted into the solid by all components, then waves can adaptively refocus at the initially launched position.

In the absence of material absorption, or the losses are small and can be negligible, the governing equations of elastic waves, e.g., SH, P-SV, and even the anelastic case as given in Eq. (22), Eq. (17) and Eq. (11), respectively, only contain a second-order time-derivative operator, that the systems hold the time reversibility. In other words, if there contains a solution  $\mathbf{u}(\mathbf{x}, t)$  to the homogeneous wave equation, which only controls the propagation, then its time-reversed counterpart  $\mathbf{u}(\mathbf{x}, -t)$  must also be a solution, i.e.,

$$\mathcal{L}\mathbf{u}(\mathbf{x}, -t) = 0. \quad (43)$$

The above system is just a backward wave equation, which controls how waves step backward, an opposite of going forward process, and mathematically explains why the time-reversed and back-propagated waves can trace back and refocus at the original source position.

Considering a single force source at  $\mathbf{x}_s$ , the illumination displacement wavefield is sampled by the array, time-reversed and retransmitted, then the backward displacement wavefield can be mathematically expressed as

$$\mathbf{u}(\mathbf{x}, t) = \sum_{\mathbf{x}_r \in \mathcal{A}} \mathbf{f}(\mathbf{x}_s, -t) * \mathbf{g}_f(\mathbf{x}_s, \mathbf{x}_r; -t) * \mathbf{g}_b(\mathbf{x}_r, \mathbf{x}; t), \quad (44)$$

where the star operator is the temporal convolution product,  $\mathbf{g}_f$  and  $\mathbf{g}_b$  denote the Green's tensors in forward and backward propagation processes, respectively, and the instrumental responses are ignored. Here if we assume the solid medium is time-invariant, which should always keep true for most geological scenarios, that two Green's tensors are the same. Taking advantage of the spatial reciprocity property (Aki & Richards 1980), the backward wavefield can spatially refocus at the original source position, i.e.,  $\mathbf{x} = \mathbf{x}_s$ , at which position the convolution between two Green's tensors in Eq. (44) is just a temporal auto-correlation function, thus the wavefield peaks, namely, at emanating time  $t = 0$ .

Using a closed cavity surrounding the source region to sample all outgoing wavefield, though is an ideal concept for refocusing, is almost impossible to realize in practical geological setting. Instead, an elastic time reversal mirror with limited array aperture is usually adopted. Due to the array aperture limitation, only a small portion of outgoing waves can be captured. In homogeneous media, the spatial resolution of time reversal refocusing is diffraction-limited (Born & Wolf 1970), that the focal spot size, i.e., the length of the first Fresnel zone, in the direction perpendicular to the array is  $\lambda \frac{L}{a}$ , and in the parallel direction is  $\lambda \left(\frac{L}{a}\right)^2$ , where  $\lambda$  is the wavelength of a time-harmonic signal,  $L$  is the distance from source to array, and  $a$  is the array aperture. Thus in the remote-sensing regime  $a \ll L$ , we can get much more better focal resolution in the perpendicular direction.

The heterogeneities give rise to the multiple scattering and multi-pathing phenomena of seismic waves propagating in heterogeneous solids, as shown in the interaction patterns depicted with the banana-doughnut traveltime sensitivity kernels in the previous section. An array can capture seismic waves scattered back by the velocity heterogeneities in the region far away off the array, thus the elastic time reversal mirror plays a role with larger effective aperture than its physical size, i.e.,  $a_e > a$ , that the Fresnel diffraction limitation is eliminated. The medium heterogeneities will not degrade refocusing but, conversely, can compress the focal spot to appear more tighter, which is the so-called super-resolution phenomenon. Moreover, such result is statistically stable for the probe signal in broadband regime, that the refocusing is independent of a particular realization of random medium (Papanicolaou et al. 2004). The studies (Blomgren et al. 2002; Fouque & Solna 2003; Borcea et al. 2003; Papanicolaou et al. 2004) have derived some analytical formulas of effective array size of acoustic time reversal mirror with some assumptions and approximations both for time-harmonic and broadband signals, and a common conclusion is that increasing the sound speed inhomogeneity can enlarge the effective array aperture thus get a better focal resolution. These observed phenomena, interpretations, and analyses achieved in the domain of acoustics are obviously applicable to SH wave, which is a type of scalar wave in the perspective of governing partial differential equation, just by replacing sound speed with shear wave velocity and observing normal displacement instead of sound pressure quantity. For the P-SV case, the situation becomes more complicated, as there are different types of waves and the conversions between each other. In this work, we are not trying to derive an asymptotic refocusing functional but will numerically illustrate how seismic waves refocus in heterogeneous solids using an elastic time reversal mirror.

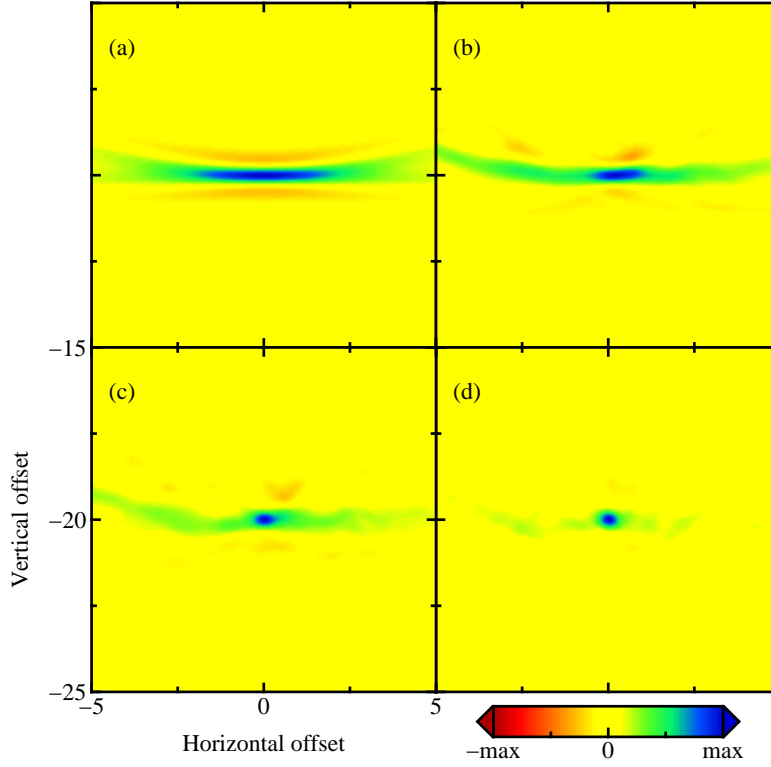


**Figure 9.** Normal displacement snapshots of time reversal SH wavefields at the refocusing time in the solids with (a) 0%, (b) 4%, (c) 8%, and (d) 12% relative standard deviations.

#### 4.2 Comparison of refocusing results in heterogeneous solids

We first investigate the SH wave refocusing in 2D heterogeneous solids characterized by the von-Kármán autocorrelation functions with different standard deviations. The SH waves are excited by a normal force source, propagate forward in the heterogeneous solids, and the particle motions in the normal direction are received by the array. The tails of the recorded signals are broadcasted first by the vibrators operating in the normal direction. Fig. 9 shows the refocused snapshots of normal displacement wavefield in the heterogeneous solids, which are zoomed in for a closer look. A broadband probe signal in the form of Ricker wavelet is adopted, thus the analytical focal resolutions are band-related and more complicated than the time-harmonic results. Comparing the subfigures (a)-(d) we can easily see that the focal spots become much more tighter in the direction parallel to the array but almost unimproved in the perpendicular direction increasing the heterogeneities. Furthermore, as shown in 12% case, the side lobes, or the second Fresnel zone, in the perpendicular direction are eliminated and the background appears smooth, that the focal spot is highlighted. The SH waves are scattered away in forward propagation but can come back in more directions, thus can refocus better in more heterogeneous solids.

Similar as the SH wave time reversal process, the elastic time reversal mirror for P-SV waves

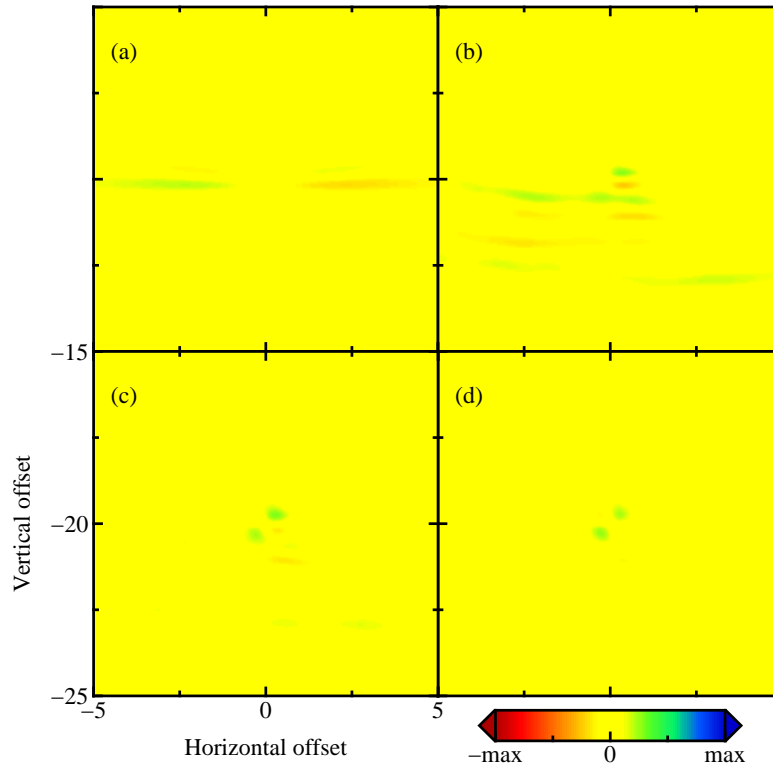


**Figure 10.** Horizontal displacement snapshots of time reversal P-SV wavefields at the refocusing time in the solids with (a) 0%, (b) 4%, (c) 8%, and (d) 12% relative standard deviations.

operates the displacement vector signals by a transceiver array, that the displacements are received, time-reversed, and retransmitted in a multi-component mode. Instead of plotting the norm values of the P-SV wavefields, the refocused displacement snapshots are decomposed in the horizontal and vertical components as given in Fig. 10 and Fig. 11, respectively. We can see that the horizontal displacement wavefields have no refocusing result, which only shows up in the snapshots of the vertical displacement components, that is because the outgoing P-SV waves are excited by a single force acting in the vertical direction. The source radiation pattern can be partially revealed by the wavefield snapshots at the refocusing time (Larmat et al. 2008; Bazargani et al. 2014). No matter there are both the compressional and shear waves, as well as the complicated conversions between each other in heterogeneous solids, the time-reversed and back-propagated P-SV waves can always refocus at the origin and the focal spots become more and more tighter in the solids with higher heterogeneities. The distorted seismograms contain the information about the response of heterogeneous solid convolved on the paths, and the time-reversed signals can be adaptively deconvolved and match the heterogeneous solid during the backward propagation. Comparing Fig. 9 and Fig. 11 we can also find that even the SH waves are in short wavelength regime and have small focal spots, the refocusing snapshots of P-SV waves appear with more cleaner backgrounds and highlighted focal spots, that is because the P-SV waves trace back

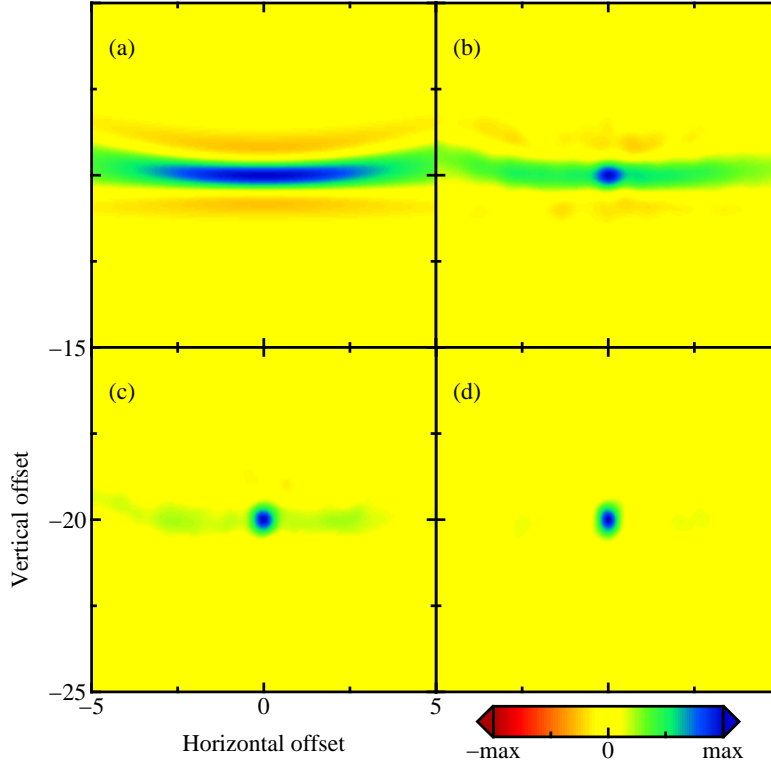


**Figure 11.** Vertical displacement snapshots of time reversal P-SV wavefields at the refocusing time in the solids with (a) 0%, (b) 4%, (c) 8%, and (d) 12% relative standard deviations.

with the superimposed contributions of compressional and shear waves, that more waves can reach the origin at the same time. The evidence can be found by comparing the banana-doughnut traveltime sensitivity kernels of SH waves shown in Fig. 7 and P-SV waves shown in Fig. 8 and Fig. 9.

## 5 CONCLUSIONS AND DISCUSSION

Through the numerical experiments we have demonstrated that seismic wave propagation is highly subject to the internal heterogeneities of solid medium that the waves become distorted when reach receivers. The seismograms recorded in heterogeneous solids exhibit the stochastic fluctuation feature, which turns out the indeterminate traveltime and amplitude information in each signal trace, or the disrupted phase delays between elements in array signal processing. The insufficient knowledge of random solid prevents us to accurately quantify the propagation response, thus decrease our ability to extract the source information, such as location and focal mechanism, using the methods based upon an assumption with a deterministic and known Green's function.

We have characterized how the seismic waves interact with the heterogeneous solids propagating from source to array by painting the banana-doughnut traveltime sensitivity kernels with the adjoint method, and shown that the seismic waves in heterogeneous solids are more sensitive to the shear

wave velocity structure, that more and more fraction is converted to shear waves. The dispersion of sensitivity kernels caused by solid heterogeneities, though can enlarge the coverage, in return requires a more denser source and receiver deployment in order to take account of the massive grains in the scattering regime. The stochastic disturbance in recorded seismograms can hold back the practicability of kernel-based tomographic inversions to get a fine resolution of the major background structures in heterogeneous solids, e.g., volcano structure imaging, especially for the full-waveform based methods.

We have illustrated that the super-resolution phenomenon also shows up for seismic waves in heterogeneous solids, no matter there are multiple types of waves and complicated conversions. With the kernel tool, we have clearly showed that the seismic waves in the heterogeneous solids can launch out in a wider-angle to the array, then the time-reversed and back-propagated wavefields can return back at origin in more directions, thus coherently highlight the focal spot. Though the focal resolution is enhanced, the heterogeneous solids can scatter seismic waves away thus decrease the absolute refocusing amplitude, but such wave energy loss can be simply compensated by amplifying the retransmitting signals. If the medium attenuation effect is unnegligible, the time-reversibility of the system can not be hold anymore, and in a changeable solid medium the spatial reciprocity is also unattainable, then more investigations are needed to examine the tolerance of refocusing with elastic time reversal mirror in these extreme conditions. In our situations, the seismic waves are broadcasted in the true solids with a physical elastic time reversal mirror, which is used to refocus seismic wave energy to a probing position while keep other place still in rest, or enhance the level of echo bounced back from a scatterer. The application of elastic time reversal mirror in source imaging is actually a numerical reproduction, that the backward propagation is performed in a fictitious numerical model. With the limited knowledge of heterogeneous solid, though some statistical moments such as mean value and variance may be available, the actual realization of the random distribution is always unknowable. The mismatch between the true heterogeneous solid and the fictitious model will lead to a noisy and unreliable refocusing image. To address the problem, Borcea et al. (2005, 2006) propose a time-reversal based imaging algorithm in acoustics, named coherent interferometry, with the adjustable decoherence parameters to achieve a good balance between the image sharpness and stability, and the method can be easily adapted to the elastic circumstance.

## ACKNOWLEDGMENTS

This work was supported by the QUEST Initial Training Network funded within the European Union Marie Curie Programme, a Science Foundation Ireland Principal Investigator Award through the Wave-Obs project, and the FUTUREVOLC project funded by the Environment programme of the FP7 programme of the European Commission. The full-waveform simulations were performed based

upon the open-source package SPEC2D, and the data was visualized with the open-source package GMT. The authors acknowledge the Irish Centre for High-End Computing for the provision of computational facilities.

## REFERENCES

- Aki, K., 1969. Analysis of the seismic coda of local earthquakes as scattered waves, *Journal of geophysical research*, **74**(2), 615–631.
- Aki, K., 1980. Scattering and attenuation of shear waves in the lithosphere, *Journal of Geophysical Research: Solid Earth (1978–2012)*, **85**(B11), 6496–6504.
- Aki, K., 1992. Scattering conversions p to s versus s to p, *Bulletin of the Seismological Society of America*, **82**(4), 1969–1972.
- Aki, K. & Richards, P., 1980. Quantitative seismology: Theory and methods, *Volume I: WH Freeman & Co.*
- Alpay, O. A. et al., 1972. A practical approach to defining reservoir heterogeneity, *Journal of Petroleum Technology*, **24**(07), 841–848.
- Bazargani, F., Snieder, R., et al., 2014. Optimal wave focusing in elastic media, in *2014 SEG Annual Meeting*, Society of Exploration Geophysicists.
- Blomgren, P., Papanicolaou, G., & Zhao, H., 2002. Super-resolution in time-reversal acoustics, *The Journal of the Acoustical Society of America*, **111**(1), 230–248.
- Borcea, L., Papanicolaou, G., & Tsogka, C., 2003. A resolution study for imaging and time reversal in random media, in *Special Session at AMS-UMI First Joint International Meeting on Inverse Boundary Problems and Applications, June 12-16, 2002, Pisa, Italy*, vol. 333, p. 63, American Mathematical Soc.
- Borcea, L., Papanicolaou, G., & Tsogka, C., 2005. Interferometric array imaging in clutter, *Inverse Problems*, **21**(4), 1419.
- Borcea, L., Papanicolaou, G., & Tsogka, C., 2006. Coherent interferometric imaging in clutter, *Geophysics*, **71**(4), SI165–SI175.
- Born, M. & Wolf, E., 1970. Principles of optics, *Moscow*.
- Chakroun, N., Fink, M., Wu, F., et al., 1995. Time reversal processing in ultrasonic nondestructive testing, *Ultrasonics, Ferroelectrics, and Frequency Control, IEEE Transactions on*, **42**(6), 1087–1098.
- Derode, A., Roux, P., & Fink, M., 1995. Robust acoustic time reversal with high-order multiple scattering, *Physical review letters*, **75**(23), 4206.
- Dziewonski, A. M. & Woodhouse, J. H., 1987. Global images of the earth's interior, *Science*, **236**(4797), 37–48.
- Fichtner, A., Kennett, B. L., Igel, H., & Bunge, H.-P., 2010. Full waveform tomography for radially anisotropic structure: new insights into present and past states of the australasian upper mantle, *Earth and Planetary Science Letters*, **290**(3), 270–280.

- Fink, M., 1992. Time reversal of ultrasonic fields. i. basic principles, *Ultrasonics, Ferroelectrics, and Frequency Control, IEEE Transactions on*, **39**(5), 555–566.
- Fink, M., 2008a. Time reversed acoustics, *Physics today*, **50**(3), 34–40.
- Fink, M., 2008b. Time-reversal waves and super resolution, in *Journal of Physics: Conference Series*, vol. 124, p. 012004, IOP Publishing.
- Fink, M. & Prada, C., 2001. Acoustic time-reversal mirrors, *Inverse problems*, **17**(1), R1.
- Fouque, J. & Solna, K., 2003. Time-reversal aperture enhancement, *Multiscale Modeling & Simulation*, **1**(2), 239–259.
- Gardner, G., Gardner, L., & Gregory, A., 1974. Formation velocity and density-the diagnostic basics for stratigraphic traps, *Geophysics*, **39**(6), 770–780.
- Hards, V., Kempton, P., & Thompson, R., 1995. The heterogeneous iceland plume: new insights from the alkaline basalts of the snaefell volcanic centre, *Journal of the Geological Society*, **152**(6), 1003–1009.
- Jackson, D. R. & Dowling, D. R., 1991. Phase conjugation in underwater acoustics, *The Journal of the Acoustical Society of America*, **89**(1), 171–181.
- Komatitsch, D. & Martin, R., 2007. An unsplit convolutional perfectly matched layer improved at grazing incidence for the seismic wave equation, *Geophysics*, **72**(5), SM155–SM167.
- Komatitsch, D. & Vilotte, J.-P., 1998. The spectral element method: an efficient tool to simulate the seismic response of 2d and 3d geological structures, *Bulletin of the seismological society of America*, **88**(2), 368–392.
- Komatitsch, D., Tsuboi, S., & Tromp, J., 2005. The spectral-element method in seismology, *Seismic Earth: Array Analysis of Broadband Seismograms*, pp. 205–227.
- Kuperman, W., Hodgkiss, W. S., Song, H. C., Akal, T., Ferla, C., & Jackson, D. R., 1998. Phase conjugation in the ocean: Experimental demonstration of an acoustic time-reversal mirror, *The journal of the Acoustical Society of America*, **103**(1), 25–40.
- Larmat, C., Montagner, J.-P., Fink, M., Capdeville, Y., Tourin, A., & Clévéde, E., 2006. Time-reversal imaging of seismic sources and application to the great sumatra earthquake, *Geophysical Research Letters*, **33**(19).
- Larmat, C., Tromp, J., Liu, Q., & Montagner, J.-P., 2008. Time reversal location of glacial earthquakes, *Journal of Geophysical Research: Solid Earth (1978–2012)*, **113**(B9).
- Liu, Q. & Tromp, J., 2006. Finite-frequency kernels based on adjoint methods, *Bulletin of the Seismological Society of America*, **96**(6), 2383–2397.
- Marquering, H., Dahlen, F., & Nolet, G., 1999. Three-dimensional sensitivity kernels for finite-frequency traveltimes: the banana-doughnut paradox, *Geophysical Journal International*, **137**(3), 805–815.
- O’Brien, G., Lokmer, I., De Barros, L., Bean, C. J., Saccorotti, G., Metaxian, J.-P., & Patané, D., 2011. Time reverse location of seismic long-period events recorded on mt etna, *Geophysical journal international*, **184**(1), 452–462.
- Papanicolaou, G., Solna, K., & Ryzhik, L., 2004. Statistical stability in time reversal, *SIAM Journal on Applied Mathematics*, **64**(4), 1133–1155.
- Patera, A. T., 1984. A spectral element method for fluid dynamics: laminar flow in a channel expansion,



- Journal of computational Physics*, **54**(3), 468–488.
- Peter, D., Tape, C., Boschi, L., & Woodhouse, J., 2007. Surface wave tomography: global membrane waves and adjoint methods, *Geophysical Journal International*, **171**(3), 1098–1117.
- Peter, D., Komatitsch, D., Luo, Y., Martin, R., Le Goff, N., Casarotti, E., Le Loher, P., Magnoni, F., Liu, Q., Blitz, C., et al., 2011. Forward and adjoint simulations of seismic wave propagation on fully unstructured hexahedral meshes, *Geophysical Journal International*, **186**(2), 721–739.
- Porter, R. P., 1989. Generalized holography with application to inverse scattering and inverse source problems, *Progress in optics*, **27**, 315–397.
- Prada, C., Wu, F., & Fink, M., 1991. The iterative time reversal mirror: A solution to self-focusing in the pulse echo mode, *The Journal of the Acoustical Society of America*, **90**(2), 1119–1129.
- Rubino, J. G. & Holliger, K., 2012. Seismic attenuation and velocity dispersion in heterogeneous partially saturated porous rocks, *Geophysical Journal International*, **188**(3), 1088–1102.
- Sato, H., Fehler, M. C., & Maeda, T., 2012. *Seismic wave propagation and scattering in the heterogeneous earth*, vol. 496, Springer.
- Stacey, R., 1988. Improved transparent boundary formulations for the elastic-wave equation, *Bulletin of the Seismological Society of America*, **78**(6), 2089–2097.
- Tanimoto, T., 1990. Modelling curved surface wave paths: membrane surface wave synthetics, *Geophysical Journal International*, **102**(1), 89–100.
- Thomas, J.-L., Fink, M., et al., 1996. Ultrasonic beam focusing through tissue inhomogeneities with a time reversal mirror: application to transskull therapy, *Ultrasonics, Ferroelectrics, and Frequency Control, IEEE Transactions on*, **43**(6), 1122–1129.
- Trampert, J. & Woodhouse, J. H., 1995. Global phase velocity maps of love and rayleigh waves between 40 and 150 seconds, *Geophysical Journal International*, **122**(2), 675–690.
- Tromp, J., Tape, C., & Liu, Q., 2005. Seismic tomography, adjoint methods, time reversal and banana-doughnut kernels, *Geophysical Journal International*, **160**(1), 195–216.
- Tromp, J., Komatitsch, D., & Liu, Q., 2008. Spectral-element and adjoint methods in seismology, *Communications in Computational Physics*, **3**(1), 1–32.
- Tsogka, C. & Papanicolaou, G. C., 2002. Time reversal through a solid–liquid interface and super-resolution, *Inverse Problems*, **18**(6), 1639.
- von Kármán, T., 1948. Progress in the statistical theory of turbulence, *Proceedings of the National Academy of Sciences of the United States of America*, **34**(11), 530.
- Warren, J., Root, P. J., et al., 1963. The behavior of naturally fractured reservoirs, *Society of Petroleum Engineers Journal*, **3**(03), 245–255.
- Wegler, U. & Lühr, B. G., 2001. Scattering behaviour at merapi volcano (java) revealed from an active seismic experiment, *Geophysical Journal International*, **145**(3), 579–592.
- Wu, S., Aki, K., Wu, R.-S., & Aki, K., 1989. *Scattering and attenuations of seismic waves*, Springer.
- Zhu, H., Luo, Y., Nissen-Meyer, T., Morency, C., & Tromp, J., 2009. Elastic imaging and time-lapse migration

based on adjoint methods, *Geophysics*, **74**(6), WCA167–WCA177.

Zhu, H., Bozdağ, E., Peter, D., & Tromp, J., 2012. Structure of the european upper mantle revealed by adjoint tomography, *Nature Geoscience*, **5**(7), 493–498.